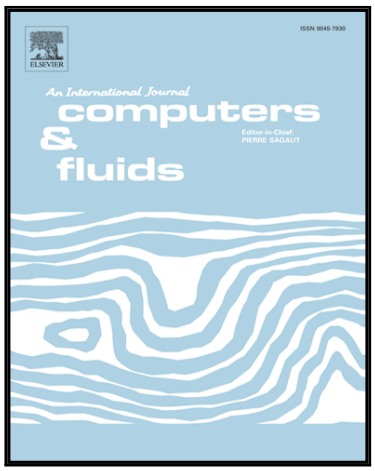

Physical insight into the accuracy of finely-resolved iLES in turbulent boundary layers

Konstantinos Ritos, Ioannis W. Kokkinakis, Dimitris Drikakis

PII: S0045-7930(17)30256-6
DOI: 10.1016/j.compfluid.2017.07.018
Reference: CAF 3551

To appear in: *Computers and Fluids*

Received date: 14 March 2017
Revised date: 5 July 2017
Accepted date: 19 July 2017

Please cite this article as: Konstantinos Ritos, Ioannis W. Kokkinakis, Dimitris Drikakis, Physical insight into the accuracy of finely-resolved iLES in turbulent boundary layers, *Computers and Fluids* (2017), doi: 10.1016/j.compfluid.2017.07.018

Highlights

- Physical insight into the accuracy of iLES methods for turbulent boundary layers.
- Order of accuracy in iLES affects turbulence anisotropy and symmetry.
- Highest anisotropy correlates with maximum Reynolds stress and minimum flatness.
- High-order iLES comparable to DNS using coarser resolution.

Physical insight into the accuracy of finely-resolved iLES in turbulent boundary layers.

Konstantinos Ritos[1,*], Ioannis W. Kokkinakis[a], Dimitris Drikakis[a]

[a] *University of Strathclyde, Glasgow, G1 1XJ, UK*

Abstract

This paper investigates the numerical accuracy of implicit Large Eddy Simulations (iLES) in relation to compressible turbulent boundary layers (TBL). iLES are conducted in conjunction with Monotonic Upstream-Centred Scheme for Conservation Laws (MUSCL) and Weighted Essentially Non-Oscillatory (WENO), ranging from 2nd to 9th-order. The accuracy effects are presented from a physical perspective showing skewness, flatness and anisotropy calculations, among others. The order of the scheme directly affects the physical representation of the TBL, especially the degree of asymmetry and anisotropy in the sub-layers of the TBL. The study concludes that high-order iLES can provide an accurate and detailed description of TBL directly comparable to available DNS and experimental results.

Keywords: iLES, High-Order, TBL, Supersonic

1. Introduction

Design processes in engineering applications require satisfying various constraints in order to adhere to design quality standards. Through careful planning and availability of instrumentation/apparatus that conform to the necessary specifications, experimental results can considerably assist during the design stage. However, most experiments are deemed cumbersome and require considerable time to plan, execute and later analyse. This is particularly true when

*Corresponding author
Email address: konstantinos.ritos@strath.ac.uk (Konstantinos Ritos)

an iterative process or optimization approach is required early on in the design phase. Furthermore, availability of diagnostic instrumentation limits the amount of useful information that can be extracted.

Computational methods offer the possibility of a high turnover of results and ample amounts of available data, allowing for a plethora of variations to the initial design of a product to be investigated. They are increasingly becoming more popular and widely used from simple low speed flows to hypersonic aerodynamics and heat transfer studies of complex geometries [1]. However, they are still treated with some caution and due care as the solutions provided can contain significant inaccuracies. For example in fluid flow simulations these are caused mostly by the number of assumptions associated with turbulence modelling as well as the excessive numerical dissipation of schemes particularly when simulations are performed on coarse grids.

In an effort to combine the high fidelity of Direct Numerical Simulation (DNS) with the computational efficiency of classical Large Eddy Simulation (LES) led to the development of implicit LES (iLES). This concept emerged from observations reported by Boris et al. [2] and has been applied successfully to model several complex flows in engineering and other fields. The use of iLES in free and wall-bounded flows has been justified by Fureby and Grinstein [3], while a validation of the method through theoretical analysis has been presented by Margolin et al. [4]. In incompressible flows, it is possible to develop an optimised stencil with regard to numerical dissipation [5], however, in the case of compressible flows the numerical method should be monotonic with respect to the thermodynamics quantities. More recently, Kokkinakis and Drikakis [6] presented iLES results of a weakly compressible turbulent channel flow, concluding that iLES can achieve near DNS accuracy while utilising significantly less computational resources. At the same time, and independently of [6], Poggie et al. [7] applied compressible iLES to study TBL flows resulting in the same conclusions.

In this paper, the accuracy of high-order, shock-capturing schemes along with any caveats, are investigated in conjunction with iLES to near-wall tur-

bulent boundary layer (TBL) flows. The effects of numerical dissipation for schemes with accuracy ranging from 2nd to 9th-order are investigated in supersonic TBL. The accuracy of each iLES variant is scrutinised through the calculation of higher-order statistics, i.e. skewness, flatness, and their direct comparison with available DNS and experimental data. The results show that higher order iLES schemes are particularly well suited for simulating TBL and also highlight their capability to provide a physical insight in near-wall supersonic flows.

2. The Simulation Case

The in-house block-structured grid code CNS3D is used to solve the Navier-Stokes equations using a finite volume Godunov-type method for the convective terms. The inter-cell numerical fluxes of the convective terms are calculated by solving the Riemann problem using the reconstructed values of the primitive variables at the cell interfaces. The reconstruction stencil is a one-dimensional swept unidirectional stencil. The Riemann problem is solved using the so-called Harten, Lax, van Leer, and (the missing) Contact (HLLC) approximate Riemann solver [8, 9]. Two different flux limiting approaches have been implemented in conjunction with the HLLC solver, namely the: (i) Monotone Upstream-centred Schemes for Conservation Laws (MUSCL) and (ii) Weighted-Essentially-Non-Oscillatory (WENO). Titarev and Toro [10] investigated the accuracy of WENO schemes with HLLC , but not within the iLES framework.

The flow physics are analysed with three variations of the iLES approach, with their accuracy ranging from 2^{nd} to 9^{th} order. In particular, these are the MUSCL piecewise linear 2^{nd}-order limiter [11] (henceforth labeled M2), the MUSCL 5^{th}-order limiter [12] (henceforth labeled M5), and the WENO 9^{th}-order scheme [13] (henceforth labeled W9). The viscous terms are discretised by a second-order central scheme. The solution is advanced in time by using a five-stage (fourth-order accurate) optimal strong-stability-preserving Runge-Kutta method [14]. Further details of the numerical aspects of the code are

L	u_∞	T_∞	M	P_∞
0.061 m	588 m/s	170 K	2.25	23.8 kPa
ρ_∞	T_w/T_∞	μ_∞	Tu	Re_L
0.488 kg/m^3	1.9	1.167×10^{-5} Pa s	3%	1.5×10^6

Table 1: Simulation parameters. u_∞, T_∞, M, P_∞, ρ_∞, μ_∞ are the freestream velocity, temperature, Mach number, pressure, density and viscosity, respectively. T_w is the wall temperature, Tu is the turbulence intensity at the inlet and Re_L is the Reynolds number based on the freestream properties and the length of the plate (L).

given in [6] and [15] and references therein.

The simulation is set up similarly to that used in the study of Poggie et al. [7] for ease of comparison with other numerical and experimental data produced under similar flow conditions. A supersonic flow over a flat plate at Mach number $M = 2.25$ that is fully turbulent in the region close to the outlet is considered. Based on the freestream properties and the length of the plate (L), the incoming flow has a Reynolds number of 1.5×10^6. Further flow parameters are given in Table 1.

Periodic boundary conditions are used in the spanwise (z) direction. In the wall-normal (y) direction, a no-slip isothermal wall (with a temperature T_w of 323 K) is used similar to [16]. High-order implementation of the boundary conditions requires fictitious cells to be added inside the wall. The velocity components on these cells are linearly extrapolated from the computational cells inside the domain. The temperature is linearly extrapolated using the specified wall temperature, while the density is calculated from the equation of state considering zero pressure gradient normal to the wall. Supersonic outflow conditions are imposed at the outlet, while far-field conditions are applied on the upper boundary opposite of the wall. A synthetic turbulent inflow boundary condition is used to produce a freestream flow with a superimposed random turbulence.

The synthetic turbulent inflow boundary condition is based upon the digital

filter (DF) method documented in [17, 18, 19, 20, 21] and, specifically validated in the framework of the present iLES code CNS3D in [20, 21]. According to DF, instead of using a white-noise random perturbation at the inlet, energy modes within the Kolmogorov inertial range scaling with $k^{-5/3}$, where k is the wavenumber, are introduced into the turbulent boundary layer. No large-scale energy modes scaling with k^4 are introduced. A cutoff at the maximum frequency of 50 MHz is applied, since the finest mesh used in this study would under-resolve higher values. The turbulence intensity at the inlet (Tu) is set as $\pm 3\%$ of the intensity of the freestream velocity. This perturbation has been found to be sufficient to trigger bypass transition and turbulence inside the simulation domain (Fig. 1).

The number of mesh points and the mesh spacing are given in Table 2. The iLES calculations are performed on relatively fine meshes but still coarser than required for DNS [7, 22]. This is highlighted in Table 2, where information about the meshes used in previous DNS studies is included for comparison and validation. The present mesh spacing (Δy) is scaled using the conventional inner variable method $\Delta y^+ = u_\tau \Delta y / \nu_w$, where $u_\tau = \sqrt{(\tau_w/\rho_w)}$ is the friction velocity, ν_w the near wall kinematic viscosity, τ_w the near wall shear stress, and ρ_w the near wall density.

	n_x	n_y	n_z	Δx^+	Δy_w^+	Δy_e^+	Δz^+
iLES	2591	277	139	9.06	0.497	6.26	8.53
DNS1[22]	1920	171	200	4.95-5.22	0.7	4.72-6.51	4.27-4.51
DNS2[22]	4160	221	440	5.58-5.86	0.7	9.42-12.35	4.75-4.99
DNS3[7]	22548	1277	1131	1.0	0.9	0.9	1.0

Table 2: Mesh parameters; n_x, n_y and n_z are the number of mesh points. The '+' sign denotes dimensionless mesh spacing, as defined for Δy^+ in the text. The subscripts 'w' and 'e' denote wall and boundary layer edge values, respectively.

In the next section, coarser meshes have been used to assess mesh convergence. However, the main analysis into the physical insight of the methods has

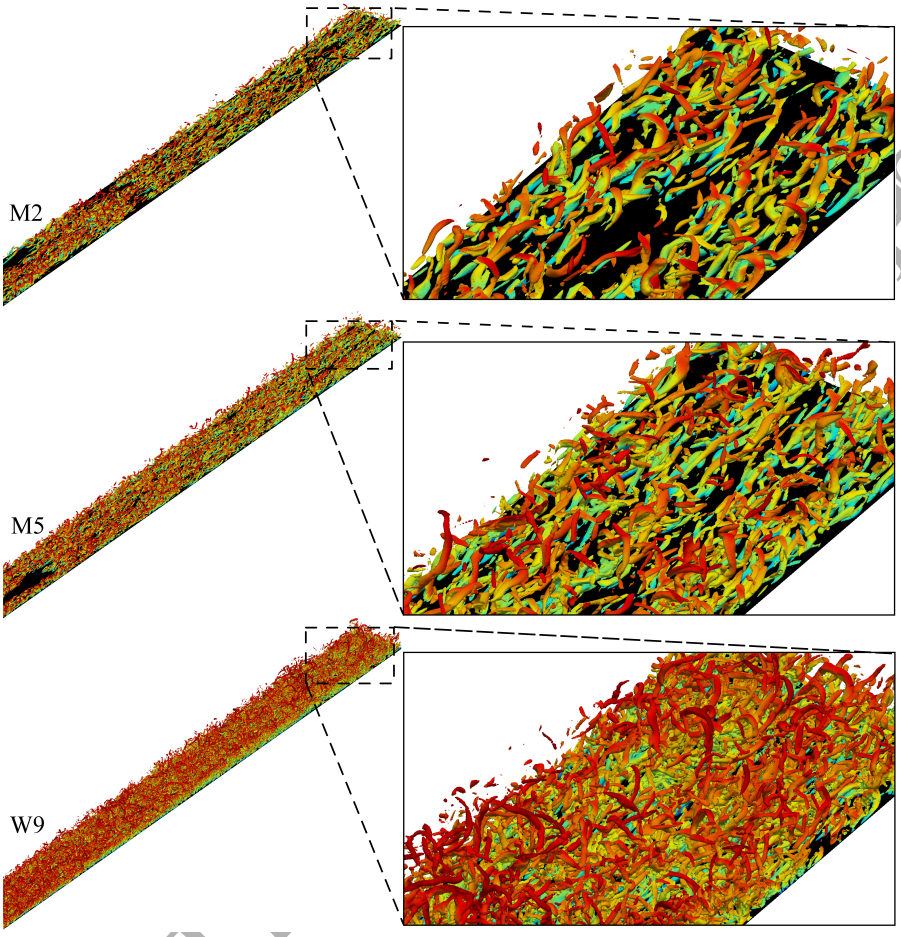

Figure 1: Iso-surfaces of Q-criterion, $Q = 2(U_\infty/\delta_0)^2$, coloured by Mach number for all iLES variants. Only a limited portion of the flow domain is shown on the left and zoom in the final 10% of the domain on the right.

been conducted by using the finest mesh resolution (see Table 2), which can be considered as an under-resolved DNS. Following this approach we were able to discern that even at finer mesh resolutions the results are dependent on the order of the scheme. Numerical stability issues associated with the W9 scheme at finer mesh resolutions require further investigation by performing resolved DNS. This is beyond the scope of the present study.

All of the calculations shown below are performed at the end of the plate in the fully turbulent region, where the boundary layer has the properties presented in Table 3. Various definitions of the Reynolds number are used in Table 3, i.e., $Re_\theta = \rho_\infty U_\infty \theta/\mu_\infty$, $Re_\tau = \rho_w u_\tau \delta/\mu_w$, and $Re_{\delta 2} = \rho_\infty U_\infty \theta/\mu_w$, to simplify the comparison of the present results with those of past and future publications. The momentum and boundary layer thicknesses are denoted by θ and δ, respectively. The flow statistics at the calculation point are computed by averaging in time over three flow cycles and spatially in the spanwise direction. The statistical convergence of the simulations based on the Standard Error of the Mean (SEM), is less than 2%. The total simulation time for each case is equal to six flow cycles, with the first three omitted from the calculations for statistical purposes. Statistical convergence in the calculations has been achieved and averaging over a longer period would not adversely impact on the accuracy. Furthermore, comparing the present results against theoretical models, DNS and experiments tested the accuracy of iLES.

	Re_θ	Re_τ	$Re_{\delta 2}$	H	M
W9	2170.0	414.0	1280.6	3.56	2.25
M5	1806.2	377.1	1065.9	3.51	2.25
M2	1593.8	344.6	940.5	3.72	2.25
DNS1[22]	1122.0	251.0	715	3.08	2.0
DNS2[22]	2377.0	497.0	1516.0	2.98	2.0
DNS3[7]	-	-	2000.0	-	2.25
Exp1[23]	4700.0	1050.0	2800	3.46	2.32
Exp2[24]	2400.0	501.0	1200.0	5.49	2.9
Exp3[25]	5100.0	1080.0	3100.0	2.00	2.28

Table 3: Boundary layer properties at the point of analysis. The same properties from previous DNS and experimental studies are also presented. The compressible form of the momentum thickness (θ) has been used. $H = \delta^*/\theta$ is the shape factor, where (δ^*) is the displacement thickness calculated for compressible flows.

3. Physical Insight into Numerical Accuracy

The assessment of the various iLES approaches begins with basic flow statistics for which a plethora of theoretical, numerical and experimental data are available. A characteristic example is the van Driest velocity profile of the TBL,

$$u_{VD} = \int_0^{u^+} \sqrt{\frac{\rho}{\rho_w}} du^+ \tag{1}$$

where the superscript '+' denotes the usual wall scaling $u^+ = u/u_\tau$. The normalised van Driest velocity profile by its value on the edge of the boundary layer is presented in Fig. 2 along with previous DNS calculations and experimental measurements. Previous publications [22, 26] have shown that for adiabatic walls a satisfactory collapse of the data is expected in the overlap layer, and also in the viscous sublayer. Small variations are expected for different Reynolds number and all present iLES calculations should appear in-between the DNS calculations of Pirozzoli et al.[22]. Only the high-order W9 satisfies this expectation and it also perfectly collapses to previous experimental measurements [24, 25].

The iLES results presented in Fig. 2 and in all of the following figures are from simulations utilising the same mesh and simulation parameters, restricting the source of any observable differences to the accuracy of the iLES variant. To support this argument and to highlight the absence of mesh resolution effects Fig. 3a shows the van Driest transformed velocity profiles for different mesh resolutions. The results on mesh G3, which consists of $\sim$ 36 million points, differ by less than 2% from those obtained by the finest mesh (G4) consisting of $\sim$ 100 million points. The average error of the present simulations in comparison to the DNS results of Pirozzoli et al.[22] is calculated using the results from Figs. 2 and 3a,

$$\varepsilon_{Avg} = \frac{1}{N} \sum_{i=1}^{N} \frac{\|\bar{u}_{DNS,i} - \bar{u}_{iLES,i}\|}{\bar{u}_{DNS,i}}, \tag{2}$$

where N is the number of points used in the calculation of the average error.

The error bars in Fig. 3b show the standard deviation of the error from its

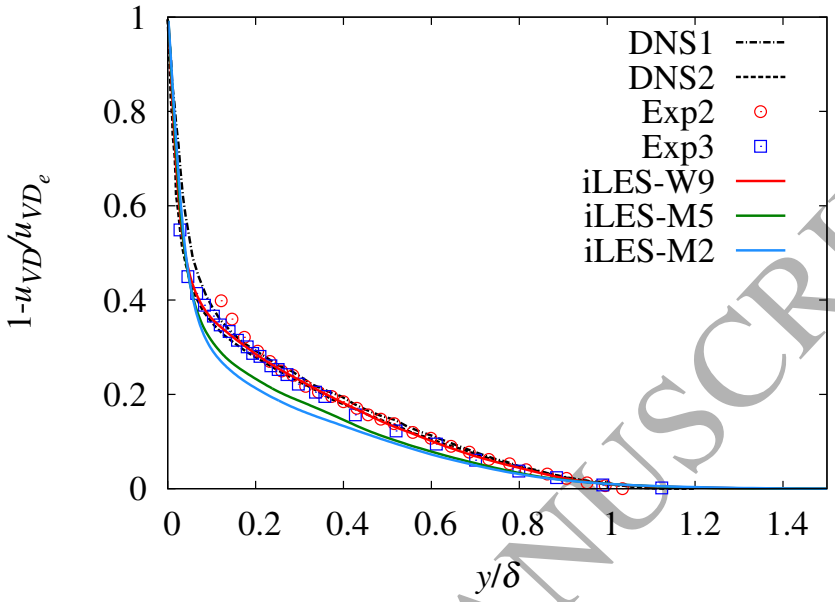

Figure 2: Comparison of van-Driest-transformed mean velocity with reference DNS and experimental data (see table 3).

average value in various points. Both the mesh size and the iLES order significantly affect the computational cost of the simulation. For each iLES variant the computational cost is normalized by the computational time of W9 on the coarsest mesh (G1). The W9 simulations on the coarser mesh G2 ($\sim$ 10.5 million mesh points) can achieve similar accuracy to the finest mesh (G4) simulations of M5 and M2, thus reducing the computational cost by approximately eight-fold. An extrapolated estimate of the computational cost that a DNS simulation would require is made based on the results of Fig. 3b using the W9 and found that the present iLES simulations are $\sim$ 5 times less computationally expensive.

Other physical features of the TBL can be studied along with the effect of the accuracy of the method on them. For example the attached-eddy hypothesis [27, 28] predicts that logarithmic layers are formed for the variance of attached variables accompanying an equilibrium layer. Perry & Li [29], based on the aforementioned hypothesis, proposed that the variance of the velocity

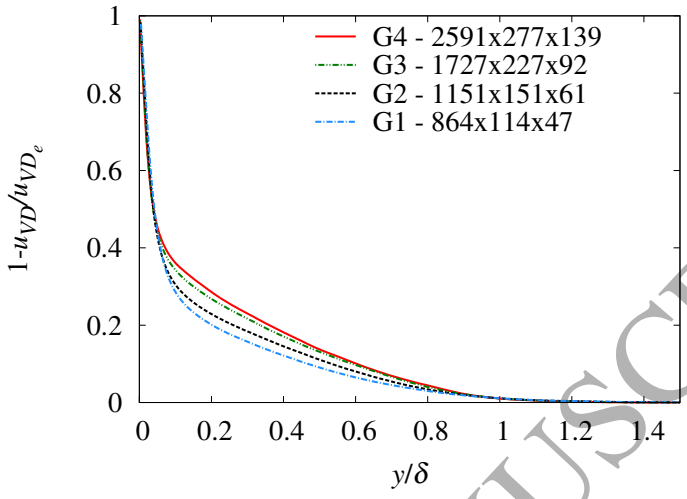

(a)

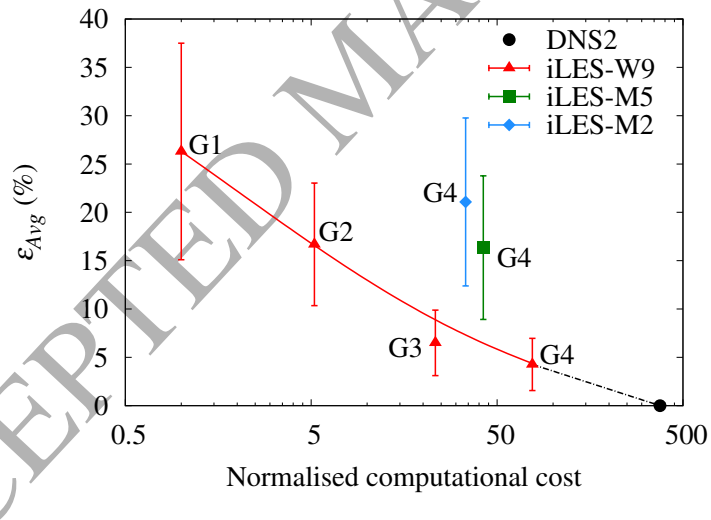

(b)

Figure 3: (a) Effect of mesh refinement on accuracy, van-Driest-transformed mean velocity, all results are from simulation utilising the W9 scheme. (b) Accuracy and computational cost comparison between different iLES variants and meshes used. The DNS simulation of Pirozzoli et al.[22] (see tables 2 and 3) has been used as the reference, error bars show the standard deviation of the values from the mean.

fluctuations should scale as

$$\frac{\overline{u_i'^2}}{u_\tau^2} = B_i - A_i log(y/\delta) - V(y^+), \tag{3}$$

where u_i' can be any of the fluctuating velocity components (u', v', or w'), $B_u = 2.39$, $A_u = 1.03$, $B_w = 1.20$. $A_w = 0.475$, while $V(y^+)$ accounts for viscous corrections. The Reynolds normal and shear stresses $\tau_{ij} = \overline{\rho u_i' u_j'}/(\rho_w u_\tau^2)$ are a common way to present the fluctuating velocity statistics (Figs. 4 and 5).

The two MUSCL variants of iLES significantly over-predict the τ_{uu} (Fig. 4a) especially the peak region in the buffer zone of the TBL. However, the highest order iLES (W9) has a very good agreement with all previous DNS results up to about $y^+ \approx 20$ where the Reynolds similarity holds [30]. Further away from the wall it is typical to observe a strong dependence on Reynolds number for results presented in inner scaling. This can explain the observed differences in the logarithmic region between the various results because the local Reynolds number is not equal. It is also notable that W9 is the only iLES variant that produces the correct scaling of τ_{uu} in the logarithmic region according to the quantitative prediction of Perry & Li [29] (Eq. 3 with $V = 0$).

The effect of the iLES order is also noticeable in the calculation of τ_{vv} where the low order schemes significantly under-predict it in the whole range of the boundary layer (Fig. 4b). This observation can be associated with unresolved turbulent scales that produce the small near-wall fluctuations. The W9 results along with the previously published DNS show a trend to Reynolds similarity for $y^+ < 40$. For higher values of y^+, the Reynolds number dependence becomes obvious.

In the presentation of τ_{ww} (Fig. 5a) the accuracy of the iLES affects only the logarithmic region, where the two MUSCL schemes under-predict the value of the normal Reynolds stress. For distances up to $y^+ \approx 30$ all simulations confirm the Reynolds independence. The present results of normal Reynolds stresses support the argument of Pirozzoli et al. [22] that turbulence dynamics over the whole TBL have an incompressible behaviour because the present observations agree very well with those made in previous publications of incompressible TBL

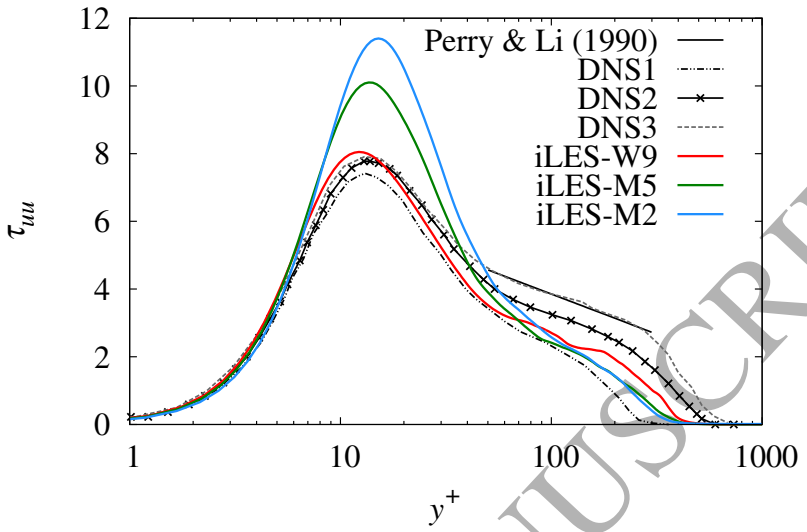

(a)

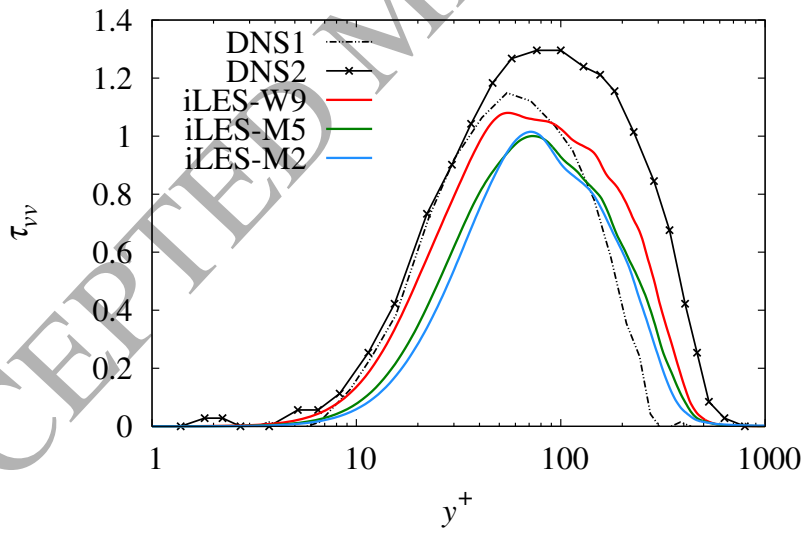

(b)

Figure 4: Comparison of Reynolds normal stresses with reference DNS and experimental data (see table 3). In 4a the quantitative scaling prediction by Perry & Li (1990) [29] is also included.

[30].

Regarding τ_{uv} in Fig. 5b, the high-order scheme W9 is in excellent agreement with the experimental measurements and previous DNS in the viscous sublayer as well as in the outer layer. The lower-order MUSCL schemes fail to achieve the same levels of accuracy in the same regions. The minimum value is in the buffer region around $y/\delta = 0.1$. In that occasion the two MUSCL schemes under-predict the trough value, while W9 slightly over-predicts it. In the logarithmic region ($0.2 < y/\delta < 0.5$) all the iLES schemes deviate from the DNS and experimental results, probably due to the mesh resolution in that region.

The effect of the iLES order on the physical representation of the TBL is further analysed by examining the skewness ($S_u = \overline{u'^3}/\overline{u'^2}^{1.5}$) and flatness (or Kurtosis) ($F_u = \overline{u'^4}/\overline{u'^2}^2$) of the streamwise velocity fluctuations, and similarly for the normal (v) and spanwise (w) components. The skewness or third moment is a measure of the asymmetry of the probability distribution of u', while flatness is the fourth moment that shows the frequency of events far from the mean value [31]. A value of skewness around zero and a value of flatness around 3 indicate a Gaussian or symmetric probability distribution function. High values of flatness indicate a highly intermittent flow. It is expected that close to the wall and in the viscous sublayer the probability distribution of the streamwise velocity fluctuations to be positively skewed, independent of the Reynolds number [22, 32, 33].

This behaviour is verified in Fig. 6a where the present iLES results are compared with previous DNS and experimental data. Flatness (Fig. 6b) is also over the Gaussian limit due to the intermittent character of turbulence in the near wall region. Skewness and flatness show a Reynolds number independence in the viscous sublayer and up to the log law region. In the buffer region the minimum flatness value is observed at the same location as that for the zero-crossing skewness ($y^+ \approx 10$) equivalently to the observation made by Österlund & Johansson [34]. At the same y^+ position the maximum normal Reynolds stress τ_{uu} is also observed, which verifies the experimental observation of Ueda & Hinze [35].

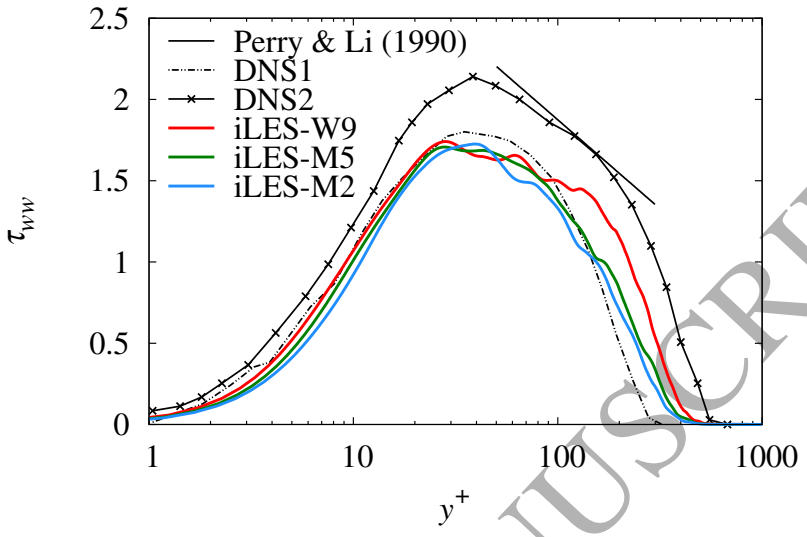

(a)

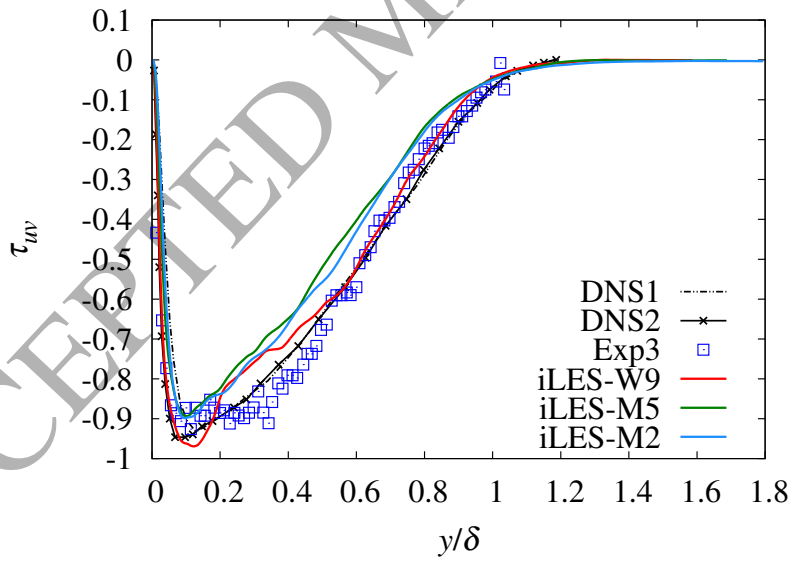

(b)

Figure 5: Comparison of Reynolds normal and shear stresses with reference DNS and experimental data (see table 3). In 5a the quantitative scaling prediction by Perry & Li (1990) [29] is also included.

Further away from the wall and in the logarithmic region of the TBL, turbulence returns to symmetry with $S_u \approx 0$ (but negative) and $F_u \approx 3$ (Fig. 6). The lower order MUSCL schemes predict a more asymmetric behaviour in contrast to W9 and previous numerical and experimental data. Close to the boundary layer edge large negative values of skewness and positive values of flatness are observed. This suggests strong intermittency in this region dominated by small negative values of u', with infrequent but intense positive values. The W9 scheme predicts with better accuracy the position of the highest asymmetry when compared to the MUSCL schemes and also providing the best accuracy over the whole boundary layer. Previous simulations conducted by the authors have shown that the mean flow quantities are not affected by the accuracy of the viscous terms discretisation. However, it still remains to investigate the effects of the discretisation of the viscous terms on high-order statistics, and this will be part of a future study.

The fluctuations of the normal component of the velocity are expected to be less skewed but with more rare events that increase intermittency. This is mirrored in the results shown in Fig. 7 where S_v is around zero up to the logarithmic layer while F_v has values greater than 3 up to the same point. M2 predicts positive values of skewness, while M5 oscillates around zero and W9 has mostly negative ones indicating a correlation of the S_v with the order the scheme. Contradicting observations regarding S_v up to the logarithmic region have been reported in the past [31, 36, 37, 38] with the W9 results being in closer agreement with the experiments of Andreopoulos et al.[36]. They reported values close to $S_v < -1$ near the wall with a cross-over to positive values at $y^+ \approx 4$.

The flatness of v' has a constant value of $F_v \sim 3$ over the log law region showing a Reynolds number and method accuracy independence (Fig. 7b). For decreasing y^+ the flatness F_v is increasing in agreement with previous numerical and experimental publications [32, 37, 38, 39]. At the boundary layer edge high levels of positive skewness and flatness are observed. This suggests strong intermittency in this region with different characteristics than those observed

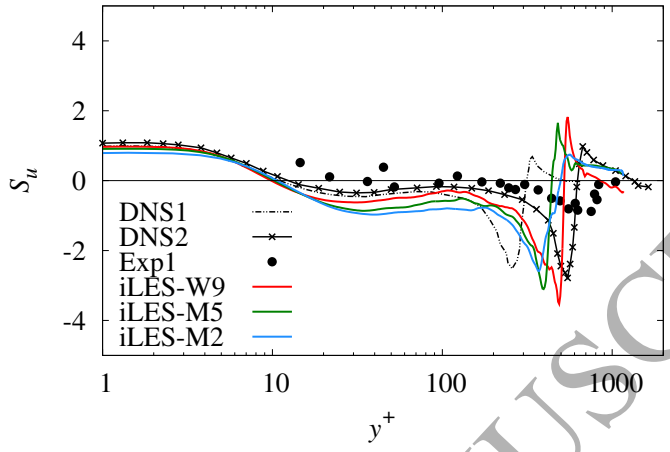

(a)

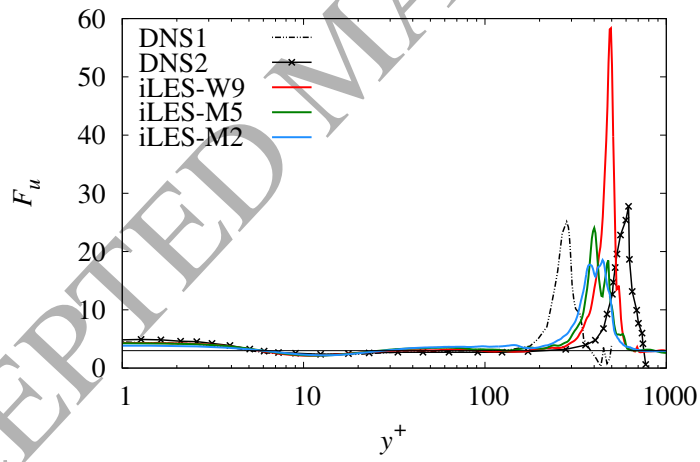

(b)

Figure 6: Comparison of streamwise velocity fluctuations (u') (a) skewness and (b) flatness between the various iLES schemes and available DNS and experimental data (see table 3). The black solid lines indicate the Gaussian limit for the high-order statistics, $S \approx 0$ and $F \approx 3$, respectively.

for u'. Specifically, Fig. 7 shows the dominance of small positive values of v', while high negative values of v' are infrequent but more intense.

It has been confirmed experimentally by Balint et al. [38] that the skewness of the spanwise component is zero in a two-dimensional boundary layer because of the symmetry of the mean flow. The present results in Fig. 8a show that w' velocity fluctuations are symmetric up to the boundary layer edge with $S_w \approx 0$ for all the variants of iLES and W9 having the smallest oscillations. Flatness has a value higher than 3 near the wall due to possible rare events while it reaches the Gaussian limit in the logarithmic layer. The high value of flatness in the viscous sub-layer has been also reported by Balint et al. [38]. Once more this component of the velocity fluctuations is highly asymmetric in the boundary layer edge as already observed for the other two components.

The three iLES variants are further scrutinised by calculating anisotropy over the TBL. In order to quantify the level of anisotropy, Lumley and Newman [40] introduced the anisotropy-invariant map (AIM). The AIM illustrates the second and third mathematical invariants (II, III) of the Reynolds stress anisotropy tensor

$$a_{ij} = \frac{\overline{u_i u_j}}{k} - \frac{\delta_{ij}}{3},\ k = \overline{u_i u_i} \tag{4}$$

with

$$II = a_{ij}a_{ji} = 2(\lambda_1^2 + \lambda_1\lambda_2 + \lambda_2^2),\ III = a_{ij}a_{in}a_{jn} = -3\lambda_1\lambda_2(\lambda_1 + \lambda_2), \tag{5}$$

where λ_i are the eigenvalues of the anisotropy tensor. The anisotropy invariants (II, III) are nonlinear functions of the Reynolds stresses leading to a distorted visual representation of anisotropy in turbulent quantities. This disadvantage of the AIM was recently tackled by Banerjee et al. [41] with the barycentric map.

According to Banerjee et al. [41] all possible anisotropy states of turbulence can be described as a convex combination of the three limiting states of componentality. These limiting states can be placed at $x_{1C} = (1, 0)$, $x_{2C} = (0, 0)$ and $x_{3C} = (1/2, \sqrt{3}/2)$ in Euclidean space. The first point x_{1C} is the one-component limit where turbulence is referred as rod-like or cigar-shaped. The second point

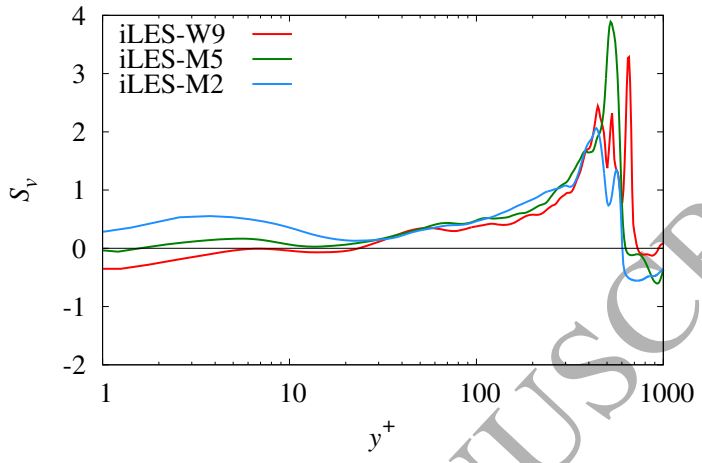

(a)

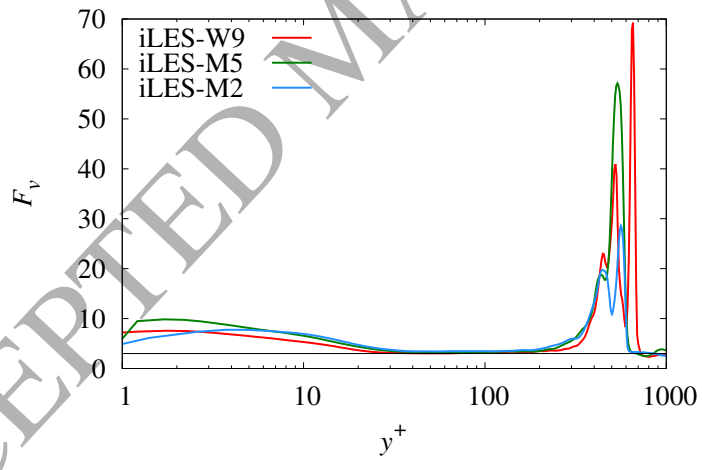

(b)

Figure 7: Comparison of normal velocity fluctuations (v') (a) skewness and (b) flatness between the various iLES schemes. The black solid lines indicate the Gaussian limit for the high-order statistics, $S \approx 0$ and $F \approx 3$, respectively.

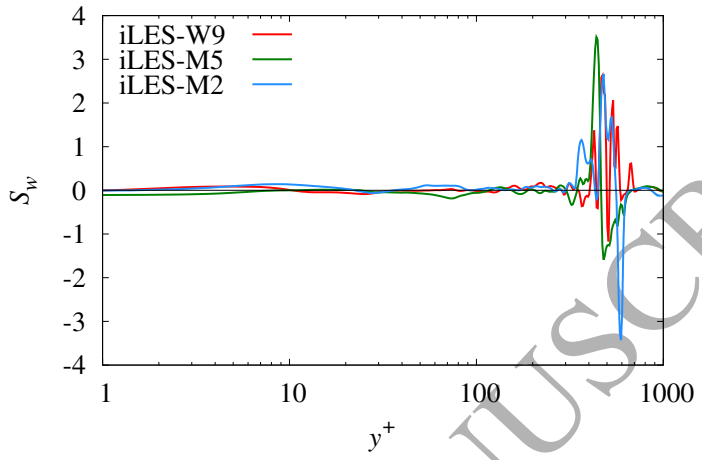

(a)

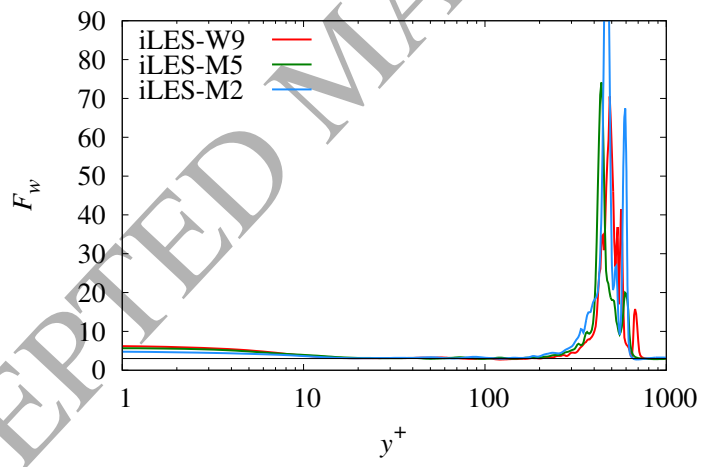

(b)

Figure 8: Comparison of spanwise velocity fluctuations (w') (a) skewness and (b) flatness between the various iLES schemes. The black solid lines indicate the Gaussian limit for the high-order statistics, $S \approx 0$ and $F \approx 3$, respectively.

x_{2C} is the two-component limit where turbulence has a disk or pancake-like shape. The final point x_{3C} indicate the three-component limit where turbulence is isotropic and can be visualised by a sphere. These limiting points form an equilateral triangle that does not introduce any visual bias of the limiting states. A coordinate system based on the eigenvalues of the anisotropy tensor can be defined such that

$$x_B = \lambda_1 - \lambda_2 + \frac{1}{2}(3\lambda_3 + 1), \tag{6a}$$

$$y_B = \frac{\sqrt{3}}{2}(3\lambda_3 + 1). \tag{6b}$$

So the barycentric map is an equivalent linear representation of the anisotropy invariants in terms of eigenvalues. The barycentric maps for each iLES scheme are given in Fig. 9. In Eq. 6 only the eigenvalues of the Reynolds stress anisotropy tensor are used to define (x_B, y_B) and as a result the barycentric map trajectories contain no information about the physical domain. To address this problem the points in Fig. 9 are coloured based on the distance from the wall (y/L). The red line indicating the base of the barycentric map denotes the two-component limit where turbulence can be visualised as an ellipse. The black solid line indicates the axisymmetric expansion limit where turbulence has a prolate spheroid shape. Similarly the blue solid line indicates the axisymmetric contraction limit where turbulence has an oblate spheroid shape. The black dashed line shows the plane strain limit where at least one of the eigenvalues is equal to zero.

All paths of anisotropy states in Fig. 9 follow approximately the same pattern, independent of the iLES scheme, which can be defined as follows for increasing y/L. Close to the wall turbulence is two-dimension having ellipsoidal shape. Because of the strong mean shear, it moves then along the $2D$-line towards the one-dimensional state, to which it is closest in the mid buffer layer around $y^+ \approx 10$. This is at the same point where the maximum τ_{uu}, minimum F_u and zero S_u coincide. Subsequently, the path follows the axisymmetric

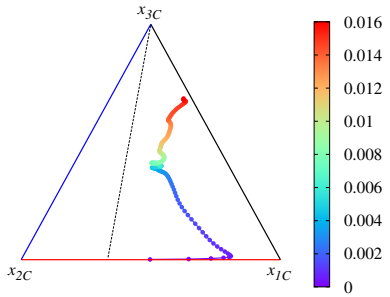

(a) M2

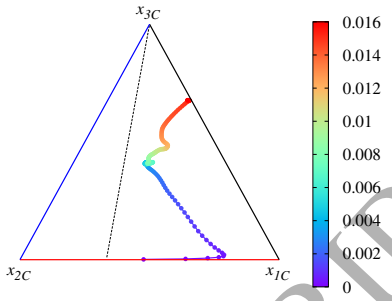

(b) M5

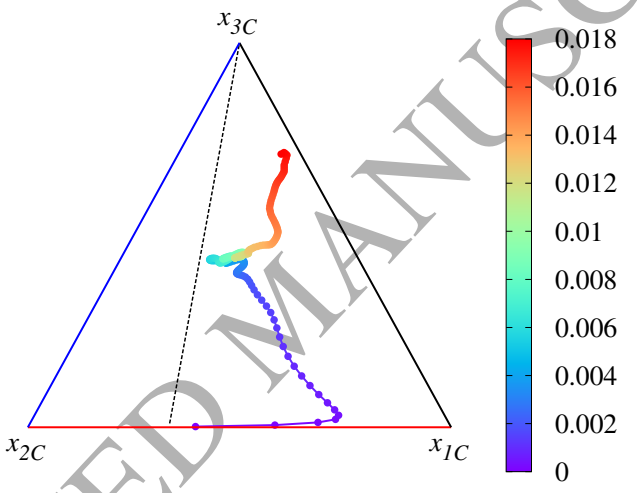

(c) W9

Figure 9: Barycentric invariance maps from all iLES schemes. The colour bar indicates the distance from the wall up to the boundary layer edge in non-dimensional units (y/L). The limiting states of componentality are labeled with "x_{1C}" for the one-component limit and "x_{2C}" for the two-component axisymmetric limit, and "x_{3C}" for the three-component isotropic limit, respectively. The red line indicates the two-component limit, the black line the axisymmetric expansion limit and the blue line the axisymmetric contraction limit, respectively. The black dashed line is the plane-strain limit.

expansion moving towards the plane strain limit, to which it is closest in the log region of the boundary layer. Turbulence keep expanding ending up on the

axisymmetric expansion limit close to an isotropic state at the boundary layer edge.

Differences between the various iLES schemes can be observed on the amount of anisotropy at each state of the path. The highest order scheme starts from a point closer to the plane strain limit compare to the other two variants. It also approach it much closer in the log region of the boundary layer. On the contrary it is the scheme that least approach the one-component limit in the mid buffer layer and at the same time produce the lowest amount of anisotropy compared to the MUSCL schemes.

4. Conclusions

This paper presented a physical insight into the accuracy of three different iLES approaches in TBL. The three iLES variants had an accuracy ranking from 2^{nd} to 9^{th} order, while the comparison was made on a relatively fine mesh of ~ 100 million points. A mesh independence study was also presented along with the effects on accuracy and performance. A mesh consisting of 1/3 the points of the finest mesh provided results less than 2% different compared to it. The W9 is not only the most accurate method of the three presented (M2, M5 and W9) on the same mesh resolution but it can also achieve superior computational efficiency when a specific level of accuracy is required. In the future, the accuracy of the present and more advanced methods, like the ADER-WENO [42, 43], can be studied in order to gain physical insight in more complex flows.

The comparison between the three iLES variants was focused on velocity statistics, including high-order ones, analysing the effect of accuracy on the symmetry and anisotropy of turbulence in each sub-layer of the TBL. A direct comparison to previous DNS and experimental data is also provided, when available, concluding to a very good agreement with the highest order iLES variant (W9).

The analysis revealed that the point of highest anisotropy in the TBL coin-

cides with the point of maximum normal Reynolds stress τ_{uu}, minimum flatness F_u and zero-crossing skewness S_u. It also supports the argument of previous publications that turbulence dynamics inside the TBL exhibit an incompressible behaviour. Near the wall and in the viscous sub-layer accuracy effects are minimal, on the contrary to the log law region of the TBL where bigger deviations were observed. Turbulence is almost isotropic at the boundary layer edge, but highly asymmetric giving high values of skewness and flatness for all velocity fluctuation components. The order of iLES accuracy affected not only the magnitude of the asymmetry and anisotropy but also the location of the extrema.

Acknowledgements

Results were obtained using the EPSRC funded ARCHIE-WeSt High Performance Computer (www.archie-west.ac.uk) under EPSRC grant no. EP/K000586/1.

References

References

[1] S. V. Utyuzhnikov, G. A. Tirskiy, Hypersonic Aerodynamics and Heat Transfer, New York,U.S.A.:Begell House, 2014.

[2] J. Boris, F. F. Grinstein, E. Oran, R. Kolbe, New insights into large eddy simulation, Fluid Dyn. Res. 10 (4-6) (1992) 199–228.

[3] C. Fureby, F. F. Grinstein, Large eddy simulation of high-reynolds-number free and wall-bounded flows, J. Comput. Phys. 181 (1) (2002) 68–97.

[4] L. G. Margolin, W. J. Rider, F. F. Grinstein, Modeling turbulent flow with implicit les, J. Turbul. 7 (15) (2006) 1–27.

[5] S. Hickel, N. A. Adams, J. A. Domaradzki, An adaptive local deconvolution method for implicit LES, J. Comput. Phys. 213 (1) (2006) 413–436.

[6] I. W. Kokkinakis, D. Drikakis, Implicit large eddy simulation of weakly-compressible turbulent channel flow, Comput. Method. Appl. M. 287 (2015) 229–261.

[7] J. Poggie, N. J. Bisek, R. Gosse, Resolution effects in compressible, turbulent boundary layer simulations, Comput. Fluids 120 (2015) 57–69.

[8] E. F. Toro, M. Spruce, W. Speares, Restoration of the contact surface in the Harten-Lax-van Leer Riemann solver, J. Shock Waves 4 (1994) 25–34.

[9] E. F. Toro, Riemann Solvers and Numerical Methods for Fluid Dynamics, 3rd Edition, Springer, 2009.

[10] V. A. Titarev, E. F. Toro, Finite-volume WENO schemes for three-dimensional conservation laws, J. Comput. Phys. 201 (1) (2004) 238–260.

[11] B. van Leer, Towards the ultimate conservative difference scheme iii. upstream-centered finite-difference schemes for ideal compressible flow, J. Comput. Phys. 23 (3) (1977) 263–275.

[12] K. H. Kim, C. Kim, Accurate, efficient and monotonic numerical methods for multidimensional compressible flows: Part ii: Multidimensional limiting process, J. Comput. Phys. 208 (2) (2005) 570–615.

[13] D. S. Balsara, C. W. Shu, Monotonicity preserving weighted essentially non-oscillatory schemes with increasingly high order of accuracy, J. Comput. Phys. 160 (2) (2000) 405–452.

[14] R. Spiteri, S. J. Ruuth, New class of optimal high-order strong-stability-preserving time discretization methods, SIAM J. Numer. Anal. 40 (2) (2002) 469–491.

[15] P. Tsoutsanis, I. W. Kokkinakis, L. Konozsy, D. Drikakis, R. J. R. Williams, D. L. Youngs, Comparison of structured and unstructured-grid, compressible and incompressible methods using the vortex pairing problem, Comput. Method. Appl. M. 293 (2015) 207–231.

[16] J. Blazek, Fluid Dynamics, Principles and Applications, Elsevier, 2015.

[17] T. S. Lund, X. Wu, K. D. Squires, Generation of turbulent inflow data for spatially-developing boundary layer simulations, J. Comput. Phys. 140 (1998) 233–258.

[18] M. Klein, A. Sadiki, J. Janicka, A digital filter based generation of inflow data for spatially developing direct numerical simulation or large eddy simulations, J. Comput. Phys. 186 (2003) 652–665.

[19] E. Touber, N. D. Sandham, Large-eddy simulation of low-frequency unsteadiness in a turbulent shock-induced separation bubble, Theor. Comp. Fluid Dyn. 23 (2009) 79–107.

[20] Z. A. Rana, B. Thornber, D. Drikakis, On the importance of generating accurate turbulent boundary condition for unsteady simulations, J. Turbul. 12 (35) (2011) 1–39.

[21] Z. A. Rana, B. Thornber, D. Drikakis, Transverse jet injection into a supersonic turbulent cross-flow, Phys. Fluids 23 (4) (2011) 1–21.

[22] S. Pirozzoli, M. Bernardini, Turbulence in supersonic boundary layers at moderate Reynolds number, J. Fluid Mech. 688 (2011) 120–168.

[23] M. Eléna, J. P. Lacharme, Experimental study of a supersonic turbulent boundary layer using a laser Doppler anemometer, J. Mec. Theor. Appl. 7 (2) (1988) 90–175.

[24] P. B. Bookey, C. Wyckham, A. J. Smits, M. P. Martin, New experimental data of STBLI at DNS/LES accessible Reynolds numbers, in: 43rd AIAA Aerospace Sciences Meeting and Exhibit, Reno, Nevada, 2005.

[25] S. Piponniau, J. P. Dussauge, J. F. Debiéve, P. Dupont, A simple model for low-frequency unsteadiness in shock-induced separation, J. Fluid Mech. 629 (2009) 87–108.

[26] A. J. Smits, J. P. Dussauge, Turbulent Shear Layers in Supersonic Flow, 2nd Edition, American Institue of Physics, 2006.

[27] A. A. Townsend, The Structure of Turbulent Shear Flow, 2nd Edition, Cambridge University Press, 1976.

[28] J. Jiménez, S. Hoyas, Turbulent fluctuations above the buffer layer of wall-bounded flows, J. Fluid Mech. 611 (2008) 215–236.

[29] A. E. Perry, J. D. Li, Experimental support for the attached-eddy hypothesis in zero-pressure-gradient turbulent boundary layers., J. Fluid Mech. 218 (1990) 405–438.

[30] H. H. Fernholz, P. J. Finley, The incompressible zero-pressure-gradient turbulent boundary layer: An assessment of the data, Prog. Aerosp. Sci. 32 (1996) 245–311.

[31] L. P. Erm, Low Reynolds-number turbulent boundary layers, Ph.D. thesis, University of Melbourne (1988).

[32] J. Kim, P. Moin, R. Moser, Turbulence statistics in fully developed channel flow at low reynolds number, J. Fluid Mech. 177 (1987) 133–166.

[33] J. Jiménez, A. Pinelli, The autonomous cycle of near-wall turbulence, J. Fluid Mech. 389 (1999) 335–359.

[34] J. M. Österlund, A. V. Johansson, Turbulence statistics of zero pressure-gradient turbulent boundary layers, Tech. rep., Sweden: KTH Mechanics (1999).

[35] H. Ueda, J. O. Hinze, Fine-structure turbulence in the wall region of a turbulent boundary layer, J. Fluid Mech. 67 (1975) 125–143.

[36] J. Andreopoulos, F. Durst, Z. Zaric, J. Jovanovic, Influence of Reynolds number on characteristics of turbulent wall boundary layers, Exp. Fluids 2 (1984) 7–16.

[37] T. G. Johansson, An experimental study of the structure of a flat plate turbulent boundary layer using Laser-Doppler velocimetry, Ph.D. thesis, Chalmers University of Technology, Göteborg (1988).

[38] J.-L. Balint, J. M. Wallace, P. Vukoslavčecvić, The velocity and vorticity vector fields of a turbulent boundary layer. part 2. statistical properties, J. Fluid Mech. 228 (1991) 53–86.

[39] P. R. Spalart, Direct simulation of a turbulent boundary layer up to $Re_\theta = 1410$, J. Fluid Mech. 187 (1988) 61–98.

[40] J. Lumley, G. Newman, The return to isotropy of homogenous turbulence, J. Fluid Mech. 82 (1977) 161–178.

[41] S. Banerjee, R. Krahl, F. Durst, C. Zenger, Presentation of anisotropy properties of turbulence, invariants versus eigenvalue approaches, J. Turbul. 8 (2007) 1–27.

[42] M. Dumbser, O. Zanotti, A. Hidalgo, D. S. Balsara, ADER-WENO Finite Volume Schemes with Space-Time Adaptive Mesh Refinement, J. Comput. Phys. 248 (2013) 257–286.

[43] O. Zanotti, M. Dumbser, Efficient conservative ADER schemes based on WENO reconstruction and space-time predictor in primitive variables, Comput. Astrophys. Cosmol. 3 (1) (2016) 1–32.